Kinetic barrier networks reveal rate limitations in ion selective membranes

Ryan S. Kingsbury[1]*†, Michael A. Baird[2], Junwei Zhang[3], Patel, Hetal[4],
Miranda J. Baran[2], Brett A. Helms[5,6], and Eric Hoek[1,7]

[1] Energy Storage and Distributed Resources Division, Lawrence Berkeley National Laboratory; Berkeley, CA, USA.

[2] Department of Chemistry, University of California, Berkeley; Berkeley, CA, USA.

[3] Department of Civil and Environmental Engineering, University of California, Berkeley; Berkeley, CA, USA.

[4] Department of Materials Science and Engineering, University of California, Berkeley; Berkeley, CA, USA.

[5] The Molecular Foundry, Lawrence Berkeley National Laboratory; Berkeley, CA, USA.

[6] Materials Sciences Division, Lawrence Berkeley National Laboratory; Berkeley, CA, USA.

[7] Department of Civil & Environmental Engineering, University of California Los Angeles; Los Angeles, CA, USA.

† Current address: Department of Civil and Environmental Engineering and Andlinger Center for Energy and the Environment, Princeton University; Princeton, NJ, USA.

* Corresponding author. Email: kingsbury@princeton.edu

Abstract

While polymer membranes are used to remove salts from environmental and industrial electrolytes, it remains a significant challenge to engineer them to isolate a single dissolved species from complex mixtures, which is important for lithium mining, battery and magnet recycling, and microelectronics. Underpinning this challenge has been a lack of understanding of rate-limiting mechanisms in selective ion transport. Here, we show that hydrated ions exhibit higher free energies of activation when crossing solution–membrane interfaces (i.e., partitioning) than when diffusing through polymers, which challenges historical assumptions embedded in widely used models of membrane performance. We further articulate a framework benchmarked with quantitative capabilities for predicting how functionality within polymer membranes or at their surfaces affects the selectivity towards individual dissolved species.

Teaser

Ions experience higher energy penalties when traversing interfaces between electrolytes and polymer membranes than when diffusing through those membranes.

Keywords

Ion exchange membranes; transition state theory; ion transport; membrane selectivity; desalination; lithium recovery; polymers of intrinsic microporosity; electrodialysis

---

Introduction

Selective polymer membranes have enabled highly successful technologies that separate dissolved ions from water, such as reverse osmosis and electrodialysis.[1–3] In reverse osmosis, a 10–100 nm thick "active layer" with a dense structure and weak charge excludes ions while permitting water to permeate when driven by a hydraulic pressure.[1,4] In electrodialysis, 50–200 μm thick ion-exchange membranes with a strong positive or negative charge exclude ions of the same charge, while permitting those of opposite charge to pass via either electrical potential or concentration gradient [3,4] Although some membranes can separate monovalent from divalent ions to a limited extent,[5–8] membranes are generally incapable of selecting for a single ionic species. Advancing ion-specific selectivity[8] would enable continuous flow membrane processes to address critical separation challenges in multiple sectors (Fig. 1A), e.g., by establishing new supplies of technologically relevant minerals, such as lithium, or harvesting scarce metals and rare earth elements from hydrolysates, sea water, or industrial wastewater. [9,10] Recent efforts have sought to achieve this by engineering the membrane polymer to include chemical functionality or particles that selectively bind the target species ("host–guest chemistry")[9,11–16] or by tuning the pore architecture using nanotubes, metal–organic frameworks, zwitterionic microchannels, or polymers of intrinsic microporosity (PIMs) [9,13,17–21] with limited success.

Engineering membranes to selectively permeate a specific ion (Fig. 1B) is challenging because membrane performance is typically understood through continuum models, such as the solution–diffusion or Nernst–Plank model,[1,4,22,23] which are disconnected from molecular-scale phenomena that influence transport of individual ions and obfuscate rate-limiting steps. Kinetic models based on Transition State Theory that connect more directly to molecular phenomena (Fig. 1C) have also been applied to membrane transport.[24–30] An early use of this approach by Zwonlinski, Eyring, and Reese[30] in 1949 concluded that diffusion through the membrane (rather than crossing the solution-membrane interface) was the rate-limiting process in most cases. As a result, studies of membrane transport today often assume (implicitly or explicitly) that diffusion is rate-limiting. However, the 1949 analysis was based on the concentration-driven transport of a single uncharged species through biological membranes in the absence of an applied pressure or electric potential driving force. Modern membrane processes involve multiple (and often charged) permeating species, charge-bearing synthetic polymers and applied driving forces, none of which were fully evaluated in this prior work. Considering that the rate-limiting step may differ among species and that charged species are likely to face a greater energy barrier than neutral ones when partitioning due to the low dielectric constant of most membranes,[31] the assumption that diffusion is generally rate-limiting must be rigorously re–examined.

Here, we develop a comprehensive kinetic modeling framework that accommodates applied driving forces and considers multiple species permeating simultaneously. Our framework treats ion transport as a network of kinetic rate processes arranged in series (for each individual species) and in parallel (with one branch per species), making it possible to identify rate-limiting steps. By measuring ionic conductivity and sorption in single and mixed alkali chloride solutions, we show that partitioning (i.e., crossing the interface) poses a significantly larger free energy barrier than diffusion in both an uncharged, yet aqueous-compatible polymer of intrinsic microporosity (AquaPIM) membrane[19] and a highly charged commercial cation exchange membrane (Fumasep FKS) that are both relevant to emerging electrochemical technologies. Our approach, which we term Barrier Network Analysis, may be used to determine whether to prioritize modification of the bulk membrane polymer (e.g., via host–guest chemistry) or surface (e.g., via coatings or functionalization) in selective membrane development.
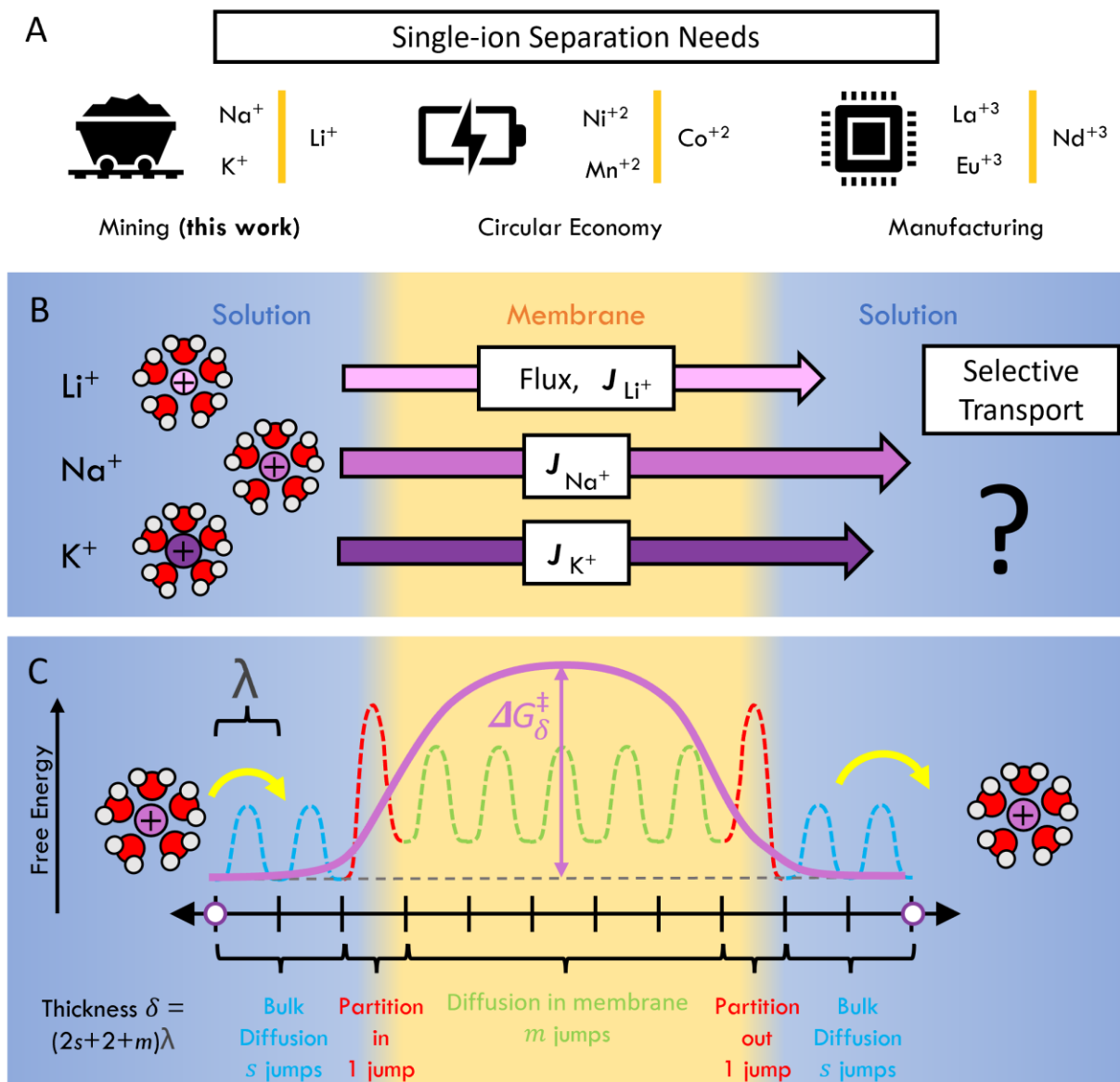
Figure 1: Analyzing polymer membranes for continuous single-ion separations. (A) Example single-ion separations that could yield metals identified as critical for multiple sectors [10]. (B) Creating membranes capable of selective transport requires engineering the flux of the target species to be greater than that of competing species. (C) We model ion permeation via a kinetic approach, in which flux can be expressed in terms of the overall membrane thickness δ and a macroscopic free energy barrier, $\Delta G_\delta^{\ddagger,o}$. $\Delta G_\delta^{\ddagger,o}$ comprises a series of microscopic energy barriers, $\Delta G^{\ddagger,o}$, associated with diffusion in electrolyte, crossing the solution–membrane interface, and diffusion within the membrane.

Theory

Kinetic barrier framework for ion transport

We first extended the original work of Zwolinski et al.[30] to derive an equation for membrane flux J (mol·m^{-2}·s^{-1}) that is valid not only for concentration-driven transport, but also for transport driven by an applied pressure or electric potential. In their model, a permeating species traverses a series of activation free energy barriers, $\Delta G^{\ddagger,o}$ (kJ·mol^{-1}), as illustrated in Fig. 1C. Energy barriers are exponentially related to the respective rate constants (k, s^{-1}) through the Eyring equation (see Supplemental Information). Our general kinetic equation for the flux of a single species is

$$J = 2k_\delta \lambda \sinh\left(\frac{\Delta W}{RT}\right)\left[\frac{C_0 - C_{n+1} + C_{n+1}\left[1 - \exp\left(\frac{-2(\Delta W)}{RT}\right)\right]}{\left[1 - \exp\left(\frac{-2(\Delta W)}{RT}\right)\right]}\right] \tag{1}$$

where k_δ (s^{-1}) is the overall macroscopic rate constant, ΔW (J·mol^{-1}) is the electrical or pressure work applied across the membrane, λ (m) is the distance between equilibrium positions, C_0 and C_{n+1} (mol·m^{-3}) are the upstream and downstream bulk species concentrations, R (8.314 J·mol^{-1}·K^{-1}) is the gas constant, and T (K) is the temperature. λ is assumed equal to 5±3 Å for all jumps in accordance with previous studies.[24,25,32–34] We present the complete derivation of Eq. 1 in the Supplemental Information, along with a discussion of various limiting cases and a complete list of the assumptions involved. Note that the Nernst–Plank equation commonly applied to ion-exchange membranes can be derived from Eq. 1 [30].

The rate constant k_δ in Eq. 1 represents the combined effect of *s* diffusion jumps in bulk solution, one jump to partition into the membrane, *m* diffusion jumps inside the membrane, and one jump to partition out of the membrane, with associated rate constants k_s, k_{sm}, k_m, and k_{ms}, respectively.[30] k_δ can be expressed in terms of these elementary rate constants as

$$k_\delta = \left[\frac{2s}{k_s} + \frac{2}{k_{sm}} + \frac{m}{Kk_m}\right]^{-1} = \frac{k_\lambda}{(2s+2+m)} \tag{2}$$

where K (dimensionless) is the partition coefficient, which is equal to the ratio of forward and reverse partitioning rate constants, i.e., $K = \frac{k_{sm}}{k_{ms}}$ (see Supplemental Information)[24,30].

Eq. 2 also shows the *microscopic* rate constant k_λ, which is the quantity that has historically been reported in kinetic studies of membrane permeation.[24,25,27,28,30,32] k_λ represents the number of times per second that a species crosses a single energy barrier, whereas k_δ, which we formulated for this work, represents the frequency of crossing the *entire membrane* (Fig. 1C). Since the membrane thickness δ (m) is much greater than λ, k_δ is slower than k_λ by a factor of $(2s + 2 + m) \approx \frac{\delta}{\lambda}$. Although both rate constants are mathematically valid when used with the correct length in Eq. 1, the macroscopic rate constant yields more intuitive results for the purpose of identifying rate-determining energy barriers, as we explain further in the Discussion.

Using the Eyring equation to replace the rate constants k in Eq. 2 with their associated free energy barriers, we can express the macroscopic free energy barrier of a species to cross the membrane, $\Delta G_{i,\delta}^{\ddagger,o}$, in terms of the energy barriers for discrete partitioning and diffusion events:

$$e^{\left(\frac{\Delta G^{\ddagger}_{i,\delta}}{RT}\right)} = \left[2se^{\left(\frac{\Delta G^{\ddagger}_{s}}{RT}\right)} + 2e^{\left(\frac{\Delta G^{\ddagger}_{sm}}{RT}\right)} + \frac{\delta}{\lambda}\frac{1}{K}e^{\left(\frac{\Delta G^{\ddagger}_{m}}{RT}\right)}\right] \tag{3}$$

To complete our kinetic framework, we consider the fact that experimentally measurable performance metrics, such as salt permeability or ionic conductivity, reflect the combined flux of multiple species. By conservation of mass, the overall flux J_{ov} must equal the sum of individual species fluxes. For the case when there is no concentration difference ($C_0 = C_{n+1}$), and assuming that the flux of each species (indicated by subscript i) is independent of other species fluxes, this sum may be expressed via Eq. 1 as:

$$J_{ov} = \sum_i |J_i| = 2\lambda \sinh\left(\frac{\Delta W}{RT}\right)\sum_i k_{i,\delta} C_i \tag{4}$$

For a solution of 1:1 salts in which the magnitude of all ion charges is equal (e.g., all monovalent ions), we may use Eq. 4 to define the *overall* free energy barrier $\Delta G_{ov,\delta}^{\ddagger,o}$, which captures the combined effects of all species permeating simultaneously:

$$\exp\left(\frac{-\Delta G_{ov,\delta}^{\ddagger}}{RT}\right) = \sum_i \frac{C_i}{C_0}\frac{\gamma_i}{\gamma_i^{\ddagger}}\exp\left(\frac{-\Delta G^{\ddagger}_{i,\delta}}{RT}\right) \tag{5}$$

where C_0 is the total salt concentration and $\frac{\gamma}{\gamma^{\ddagger}}$ is the ratio of the activity coefficient of the ion in the bulk to that of the transition state, which we assume is approximately equal for all species. A complete derivation is provided in the Supplemental Information.

Together, Eqs. 3 and 5 define quantitative relationships between the experimentally-measurable barrier $\Delta G_{ov,\delta}^{\ddagger,o}$ and the discrete partitioning and diffusion barriers associated with each permeating species. Under the assumption that species fluxes are independent (i.e., neglecting ion–ion interactions), they make it possible to model membrane transport as a network of activation energy barriers arranged in series and parallel.

With careful experimental design, and subject to certain assumptions, Barrier Network Analysis can identify kinetic rate limitations for individual ions, as we demonstrate next.

Results

Characterization of ion transport in single and mixed salt solutions

We analyzed the permeation of four ionic species—Li$^+$, Na$^+$, K$^+$, and Cl$^-$—through membranes in contact with LiCl, KCl, NaCl, and a mixture of all three salts ("NLKCl"), thus defining a system of four equations and four unknowns that makes it possible to estimate single-ion free energy barriers, as will be detailed later. We first obtained the macroscopic activation entropy $\Delta S_{ov,\delta}^{\ddagger,o}$ and enthalpy $\Delta H_{ov,\delta}^{\ddagger,o}$ for ion permeation by fitting Arrhenius-type plots of ionic conductivity vs. temperature (see Methods, Fig. 2A, S1, S2).
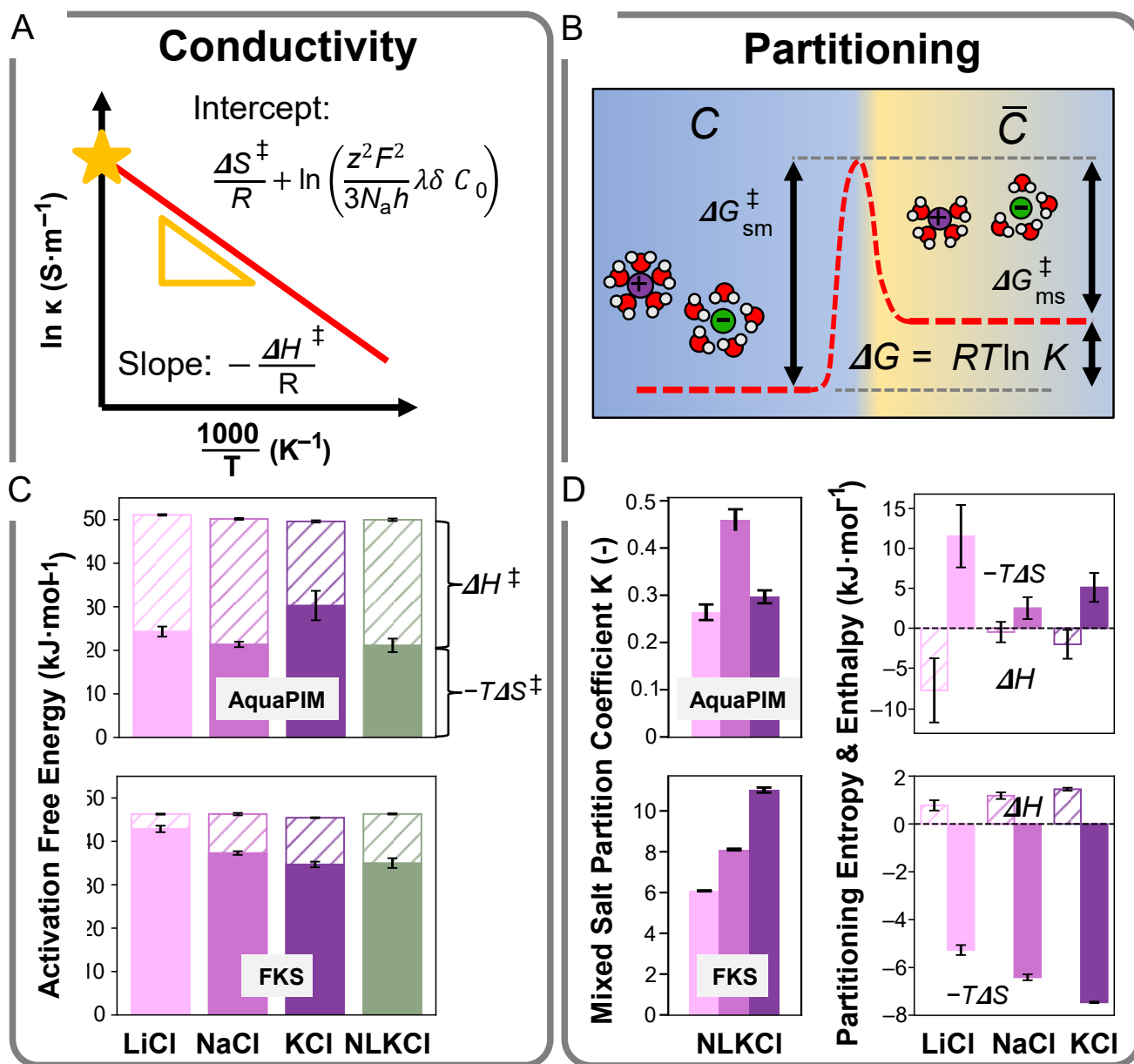
Figure 2: Characterization of alkali chloride transport in AquaPIM and FKS membranes. (A) Macroscopic activation entropy and enthalpy were obtained from the intercept and slope, respectively, of Arrhenius-type plots of conductivity vs. temperature data. Data for AquaPIM and FKS are shown panel (C). (B) Illustration of partitioning as a kinetic process mediated by forward and reverse activation free energies $\Delta G_{sm}^{\ddagger,\mathbf{o}}$ and $\Delta G_{ms}^{\ddagger,\mathbf{o}}$. (D) Measured partition coefficients of cations at 25 °C (left) and total change in entropy and enthalpy (right) for partitioning into AquaPIM and FKS in mixed salt solution. In all panels, light, medium, and dark purple bars represent Li, Na, and K salts or ions, respectively. All measurements were performed in solutions with 0.1 M total cation concentration. Error bars represent the standard error of 3–5 replicates.

The obtained free energy barriers for ion permeation through uncharged AquaPIM membranes (Fig. 2C, Table S3) were all approximately 50 kJ·mol^{-1}. Single-salt barriers varied over a 1.5 kJ.mol^{-1} range and followed the trend LiCl > NaCl > KCl, while the mixed salt barrier was intermediate between those of NaCl and KCl. For the highly charged commercial cation exchange membrane (FKS), $\Delta G_{ov,\delta}^{\ddagger,o}$ was nearly identical for LiCl, NaCl, and NLKCl at 46.3 kJ.mol^{-1}, while the energy barrier for KCl was 45.5 kJ.mol^{-1} (Fig. 2C). The ~4 kJ·mol^{-1} lower barriers in FKS compared to AquaPIM were consistent with the fact that FKS was found to have ~10x the room temperature conductivity of AquaPIM in an independent set of measurements obtained by stacking multiple membranes (Fig. S15, S16).

Activation entropies were all negative, with $-T\Delta S_{\delta}^{\ddagger,o}$ comprising 45% to 60% of the magnitude of $\Delta G_{ov,\delta}^{\ddagger,o}$ for AquaPIM, and 75% to 90% for FKS at $T = 298$ K (Fig. 2C, Table S3). In single salt solutions, the magnitude of the activation entropy for AquaPIM followed the trend KCl > LiCl > NaCl, whereas the magnitude of the activation entropy for FKS followed the trend LiCl > NaCl > KCl. For both membranes, $-T\Delta S_{\delta}^{\ddagger}$ in mixed salt solution was similar to the single-salt value with the smallest magnitude, which could indicate that permeation from mixed electrolytes favors the salt with the smallest activation entropy.

We next measured equilibrium salt partition coefficients K, which are defined as the ratio of membrane to bulk salt concentration, or in kinetic terms as the ratio of forward and reverse partitioning rate constants (Fig. 2B):[24,30]

$$K = \frac{\bar{C}}{C} = \frac{k_{sm}}{k_{ms}} = \frac{\gamma}{\bar{\gamma}}\exp\left(\frac{\Delta G_{ms}^{\ddagger} - \Delta G_{sm}^{\ddagger}}{RT}\right) \tag{6}$$

where C and $\bar{C}$ are the bulk and membrane phase salt concentrations (mol.L^{-1} of swollen membrane).[35]

In single salt solutions, room temperature partition coefficients of cations (Table S4, Fig. S10, S11) followed the same trend in both membranes (LiCl > NaCl > KCl). These trends changed in mixed salt solutions (Fig. 2D), where AquaPIM partition coefficients followed the trend KCl < LiCl < NaCl and FKS partition coefficients followed the trend KCl > NaCl > LiCl. Note that for FKS we report the *total* partition coefficient of cations, which includes both cations that neutralized the fixed charge sites on the membrane as well as mobile cations. Although it is more common to report the mobile salt partition coefficient, in the context of our kinetic treatment it is appropriate to include all cations in $\bar{C}$.

We next performed additional mixed-salt partitioning experiments at elevated temperatures and constructed Arrhenius-type plots to extract the total change in free energy, enthalpy, and entropy (e.g., $\Delta G = \Delta G_{sm}^{\ddagger} - \Delta G_{ms}^{\ddagger}$, Fig. 2B) for partitioning. For AquaPIM, entropy and enthalpy changes were all negative (–2.5 to –11.5 kJ·mol^{-1} and –0.5 to –7.5 kJ·mol^{-1}, respectively; Fig. 2D, S5, S6, Table S4). For FKS, partitioning entropies and enthalpies were all positive (5 to 8 kJ·mol^{-1} and <2 kJ·mol^{-1}, respectively) and increased in the order LiCl < NaCl < KCl. The opposite signs of entropy and enthalpy in the two membranes are likely related to charge. In FKS, charged sulfonate groups may coordinate with counter-ions, replacing water molecules from their hydration shells and causing a substantial increase in entropy. Meanwhile, stabilization of the ions could result in release of heat, explaining the positive enthalpy change. Neither effect would occur in uncharged AquaPIM.

Identifying rate limitations via barrier network analysis

We now use our characterization data to construct a kinetic barrier network representing mixed alkali chloride transport through each membrane. The central assumption in our approach is that individual energy barriers ($\Delta G_m^{\ddagger,o}$, $\Delta G_{sm}^{\ddagger,o}$, etc.) for each species are similar in both single-salt and mixed–salt experiments, which means that we neglect ion–ion interactions in the solution and the membrane. We justify this assumption by the following: 1) ions can permeate independently from one another in electrically-driven transport [36], in contrast to concentration-driven transport where ions must diffuse in pairs as "mobile salt"; 2) LiCl, NaCl and KCl are 80–95% dissociated in 0.1 M solution [37,38]; and 3) any contact ion pairs present will be uncharged and hence not transported by the electric field. We also note that our neglect of ion–ion interactions is consistent with the widely-used Nernst–Plank modeling framework. With the assumption of independent ion fluxes, we can use Eq. 5 to express our four measured values of $\Delta G_{ov,\delta}^{\ddagger,o}$ in terms of 4 unknown single-ion barriers, $\Delta G_{i,\delta}^{\ddagger,o}$, according to a system of equations:

$$
\begin{bmatrix}
\exp\dfrac{-\Delta G_{ov,LiCl}^{\ddagger,o}}{RT} \\[2mm]
\exp\dfrac{-\Delta G_{ov,NaCl}^{\ddagger,o}}{RT} \\[2mm]
\exp\dfrac{-\Delta G_{ov,KCl}^{\ddagger,o}}{RT} \\[2mm]
\exp\dfrac{-\Delta G_{ov,NLKCl}^{\ddagger,o}}{RT}
\end{bmatrix}
=
\begin{bmatrix}
1 & 0 & 0 & 1 \\
0 & 1 & 0 & 1 \\
0 & 0 & 1 & 1 \\
\frac{1}{3} & \frac{1}{3} & \frac{1}{3} & 1
\end{bmatrix}
\begin{bmatrix}
\exp\dfrac{-\Delta G_{Li^+,\delta}^{\ddagger,o}}{RT} \\[2mm]
\exp\dfrac{-\Delta G_{Na^+,\delta}^{\ddagger,o}}{RT} \\[2mm]
\exp\dfrac{-\Delta G_{K^+,\delta}^{\ddagger,o}}{RT} \\[2mm]
\exp\dfrac{-\Delta G_{Cl^-,\delta}^{\ddagger,o}}{RT}
\end{bmatrix}
\qquad (7)
$$

where each $\Delta G_{i,\delta}^{\ddagger,o}$ comprises three individual $\Delta G^{\ddagger,o}$ values corresponding to partitioning and diffusion events and one partition coefficient K (see Eq. 3), for a total of 16 unknown activation energy barriers.

Diffusion energy barriers $\Delta G_s^{\ddagger,o}$ and $\Delta G_m^{\ddagger,o}$ can be computed from the relation $D = 1/6\ k\lambda^2$ [24,30,39] using single-ion diffusion coefficients in bulk solution (Table S1) and in the membrane, respectively, eliminating eight unknowns. Note that the obtained $\Delta G_s^{\ddagger,o}$ values (12–13.7 kJ·mol^{-1}) for ion diffusion are lower by definition than more commonly reported Arrhenius activation energies (E_a; e.g., 16–21 kJ·mol^{-1})[40], because the latter values consider only activation enthalpy (See illustration in Fig. 2A). Membrane phase diffusion coefficients (Table S2) were estimated from water uptake using the Mackie–Meares model [41,42] and were similar in magnitude to the diffusion coefficient of Li$^+$ measured by NMR in a similar PIM membrane (7×10^{-10} m^2·s^{-1}),[43] indicating that the model is reasonably accurate for AquaPIM.

Measured partition coefficients for the four salts (Fig. S10, S11) eliminate an additional four unknowns, because partition coefficients for salts are equal to those of the corresponding single cations, while partition coefficients for Cl$^-$ were calculated from the concentrations of mobile salt only (i.e., excluding cations that neutralize the fixed charge groups on the FKS membrane; see Methods and Fig. S7, S8). Hence, the four K values we measured yield K_{Li^+}, K_{Na^+}, K_{K^+}, and K_{Cl^-}.

Altogether, we are left with four unknown values of the partitioning barrier $\Delta G_{sm}^{\ddagger,o}$ (one per species), which can be solved numerically using the four known values of $\Delta G_{ov,\delta}^{\ddagger,o}$. We achieved a solution with a

mean squared error of less than 0.2 kJ·mol^{-1} in $\Delta G_{ov,\delta}^{\ddagger,o}$ for both membranes, suggesting that our assumptions are reasonable for the systems studied. We estimate the maximum uncertainty in the solved $\Delta G_{i,\delta}^{\ddagger,o}$ and $\Delta G_{sm}^{\ddagger,o}$ at ±0.3 and ±0.5 kJ·mol^{-1}, respectively, based on the propagated uncertainty arising from: 1) the standard errors in our experimental activation free energy and partition coefficient measurements and 2) a deliberately large assumed range of ±3 Å in the jump length λ. Estimated uncertainties in $\Delta G_s^{\ddagger,o}$ and $\Delta G_m^{\ddagger,o}$ are larger —±3 kJ·mol^{-1}— due to the large uncertainty in λ values we considered. Additional details of the numerical solution procedure are provided in the Supplemental Information. Fully-resolved kinetic barrier networks for AquaPIM and FKS are shown in Fig. 3A and S12, respectively.

Strikingly, we find the partitioning barriers for the cations (i.e., $\Delta G_{sm}^{\ddagger,o}$ or $\Delta G_{ms}^{\ddagger,o}$) have 2–5 times the magnitude of the diffusion barriers in both uncharged AquaPIM and highly-charged FKS. For AquaPIM, $\Delta G_{sm}^{\ddagger,o} > \Delta G_{ms}^{\ddagger,o}$ because $K < 1$, and hence, the barrier to partitioning into the membrane, $\Delta G_{sm}^{\ddagger,o}$, is the largest barrier (see Eq. 6). For FKS on the other hand, $K \gg 1$ for the cations, and hence, $\Delta G_{sm}^{\ddagger,o} < \Delta G_{ms}^{\ddagger,o}$, making the barrier to partitioning *out* of the membrane the largest. The barriers associated with (de)partitioning of cations in both membranes follow the trend Li$^+$ > Na$^+$ > K$^+$, matching trends in hydration free energy and hydrated size (see Table S1).

For Cl$^-$ in AquaPIM, the partitioning barrier has a larger magnitude than the diffusion barrier and $\Delta G_{sm}^{\ddagger,o} > \Delta G_{ms}^{\ddagger,o}$ because $K < 1$, similar to the cations. In contrast, in FKS we find membrane diffusion to be rate limiting. The Cl$^-$ barrier network is striking because the overall barrier for permeation ($\Delta G_{Cl,\delta}^{\ddagger,o}$) is 50.8 kJ·mol^{-1}, the largest among all the ions, even though the largest individual barrier (diffusion) has a magnitude of just 18.6 kJ·mol^{-1} (Fig. S12). Physically, this large overall barrier reflects the preferential transport of cations due to Donnan exclusion in a membrane with a strong negative charge. Mathematically, it illustrates the combined effect of many small barriers according to Eq. 3. For the FKS membrane with a thickness of ~75 μm, m is on the order of 10^5. Hence, a sufficiently large number of 18.6 kJ·mol^{-1} barriers, coupled with $\Delta G_{sm}^{\ddagger,o} > \Delta G_{ms}^{\ddagger,o}$, can result in a large magnitude of $\Delta G_{ov,\delta}^{\ddagger,o}$. This point underscores the subtlety of determining rate limitations in polymer membranes, which we elaborate in the Discussion section.

We next performed electrodialysis experiments on mixed salt solution (see Methods and Fig. 3B) to evaluate the predictive power of barrier network analysis for ion selectivity in electrically-driven separations. We predicted the flux of each cation by using the associated $\Delta G_{i,\delta}^{\ddagger,o}$ value in Eq. 1, then computed the transport numbers according to $t_i = J_i / \sum_i J_i$. These predictions were qualitatively consistent with experimental values for cations under the assumption that Li$^+$, Na$^+$, K$^+$, and Cl$^-$ were the only transporting species (Fig. 3C) and showed reasonable quantitative agreement for the FKS membrane. Cl$^-$ ions carried a larger fraction of current than predicted by the energy barriers in Fig. 3A and S12. This is most likely a result of H$^+$ transport competing for cation transport due to pH changes in the feed solution (see Methods). Unaccounted-for H$^+$ transport would decrease the cation transport numbers and increase the experimental t_{Cl} because it was determined as 1 minus the sum of cation transport numbers.
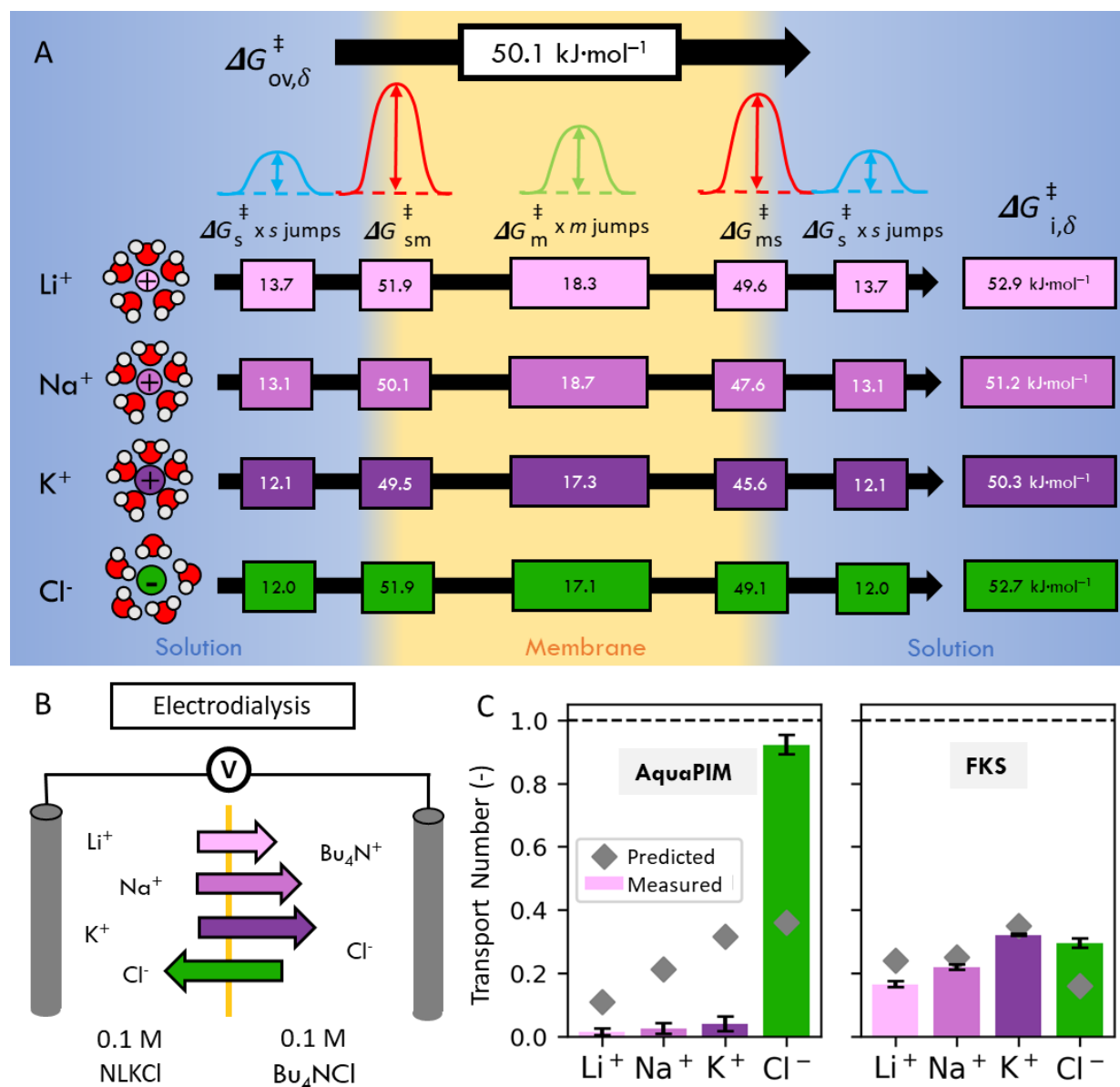
Figure 3: Barrier network analysis of alkali cation transport. (A) Fully solved kinetic barrier network representing ion transport through AquaPIM in mixed alkali chloride (NLKCl) solution. Each box shows a $\Delta G^{\ddagger,o}$ in kJ·mol^{-1}. Overall barriers for each species $\Delta G^{\ddagger,o}_{i,\delta}$ are shown to the right, while the experimentally-measurable overall energy barrier $\Delta G^{\ddagger,o}_{ov,\delta}$ is shown at the top. $\Delta G^{\ddagger,o}_{s}$ and $\Delta G^{\ddagger,o}_{m}$ values represent single energy barriers, which are repeated s and m times, respectively. Solving the barrier network using experimental data indicates that partitioning into the membrane ($\Delta G^{\ddagger,o}_{sm}$) is the process with the highest energy barrier for all ions. (B) Electrodialysis experiments using applied electric potential to drive cations through the membrane. The flux of each ion was determined using inductively coupled plasma optical emission spectrometry on the receiving solution. Bu_4N^+ = tetrabutylammonium cation. (C) Measured ion transport numbers from electrodialysis experiments (bars) vs. transport numbers predicted by the $\Delta G^{\ddagger,o}_{i,\delta}$ obtained from barrier network analysis (diamonds).

Rationalizing Results via Dehydration and Confinement

Ion dehydration, which presumably occurs during partitioning, is recognized as a key mechanism involved in ion transport through confined spaces such as polymer membranes, 2D materials, and metal organic frameworks,[16,22,34–38] and the trends we observed in the partitioning barriers for cations are qualitatively consistent with trends in bulk hydration free energy (Fig. 5a, Table S1).

To investigate whether our observations could be explained by partial ion dehydration, we used Density Functional Theory (DFT) simulations to determine the effective sizes of fully and partially dehydrated ions (Fig. 4A), which we compared to the pore size of AquaPIM, whose relatively rigid backbone results in a well-defined microporous structure.[21] Simulated ion size results (Fig. 4B) suggest that all ions must dehydrate to $n = 5-8$ H_2O molecules in order to fit inside the largest pores of AquaPIM, whereas nearly full dehydration (0−1 H_2O) would be needed for ions to fit into the 5.6 Å pores.

We next computed the changes in free energy and entropy associated with transferring the fully hydrated ion into a low dielectric environment representing the polymer membrane ($\epsilon = 5$ or 25)[44] and simultaneously removing different numbers of water molecules. The number of hydrating water molecules corresponding to full hydration of each ion was determined as the value which best reproduced the experimental solvation entropy and free energy (see Methods). Partial dehydration of cations from the fully hydrated state to $n = 5 - 8$ increases free energy 10−50 kJ·mol^{-1}, with larger increases for $\epsilon = 5$ compared to $\epsilon = 25$, while increasing the entropy by 20−70 kJ·mol^{-1} (Fig. 4D-E, solid lines, Fig. S22). We note that entropy changes were not sensitive to the dielectric environment into which the dehydrated ion was placed (Fig. S23), and that the positive entropy change is consistent with commonly observed entropy increases in spontaneous ion pairing, chelation, and precipitation reactions due to the release of free water molecules[39] and with the negative solvation entropy of bare ions (see Table S1).

Since we observed a *decrease* in entropy during ion permeation and partitioning (Fig. 2), our results cannot be explained solely by dehydration, and other factors such as confinement must play a role. Entropic activation barriers may be related to the amount of steric hindrance or confinement in the membrane, which limits the number of configurations or microstates a (partially) hydrated ion can adopt.[16] Our data supports this idea, because observed trends in single-salt $T\Delta S_\delta^{\ddagger}$ were roughly consistent with the trends in water uptake (i.e., lower water uptake equals higher activation entropy; see Fig. S3 and S4), indicating that the large activation entropies are related to confinement that occurs as ions partition into the membrane. Furthermore, negative activation entropies are typically associated with slow reaction steps in bulk chemical reactions;[45] therefore, identifying the cause of the negative entropy changes we observed should yield insight into the rate-limiting transport phenomenon.
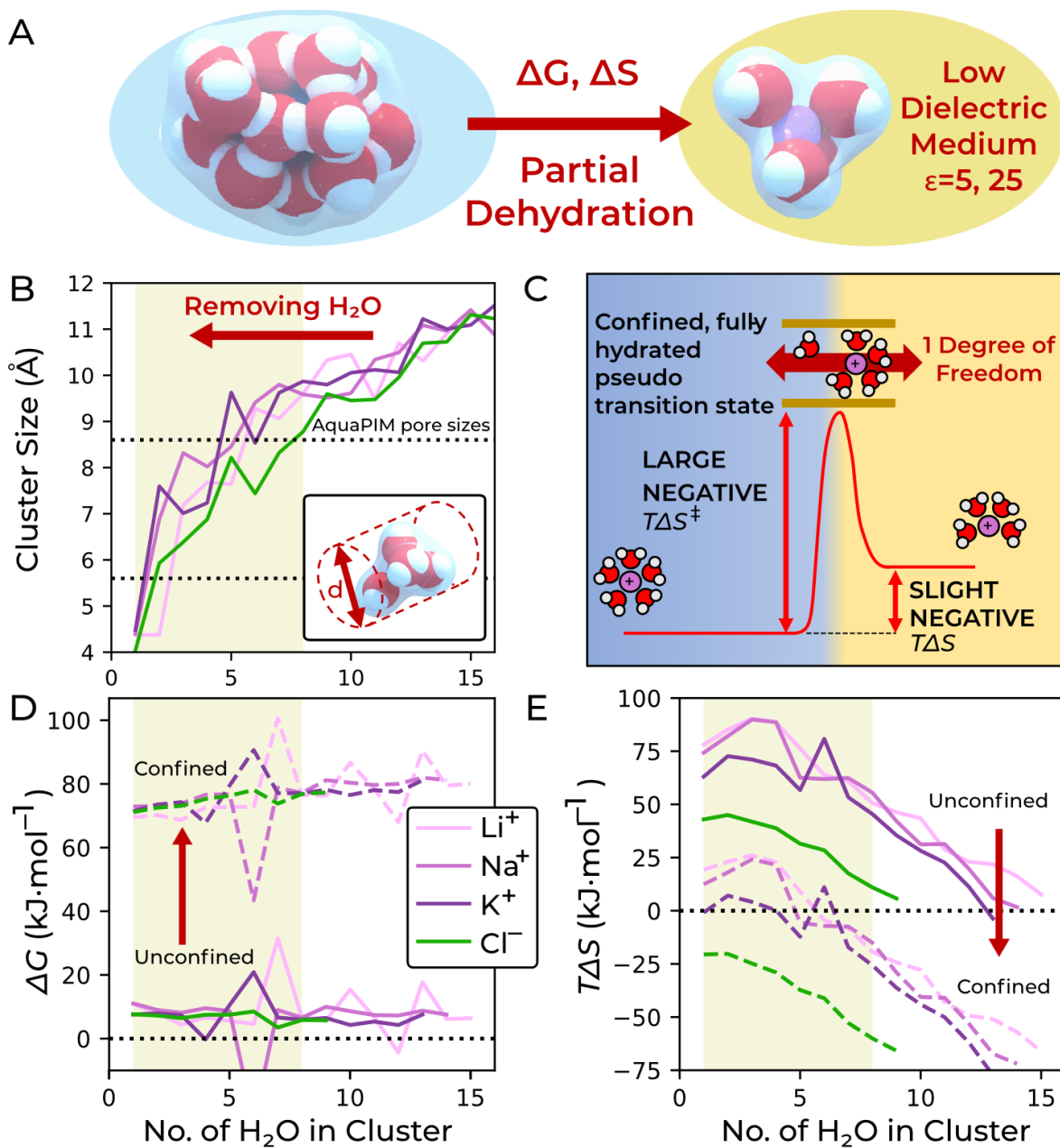
Figure 4: Molecular simulation of partial ion dehydration. (A) Schematic illustration of the partial dehydration reaction with accompanying transfer to a lower-dielectric environment. (B) Change in enclosing diameter vs. no. of H_2O molecules in the cluster (where the rightmost value corresponds to the fully hydrated state) for each ion. Dashed lines indicate the predominant pore diameters in AquaPIM membranes.[21] (C) Schematic of hypothesized mechanism of ion permeation in which hydrated ions pass through a confined pseudo-transition state in which their translational motion is restricted to just one degree of freedom. (D) Change in free energy and (E) change in entropy, $T\Delta S$, associated with partial dehydration from bulk solution into a polymer with permittivity $\epsilon = 25$. Solid lines are calculated without confinement; dashed lines are calculated with confinement to 1 degree of freedom. In panels (B), (C), and (E), shading indicates the range of n H_2O values that would allow ions to fit in the pores of AquaPIM, and the lines are colored according to the legend in panel (D).

To evaluate whether confinement could explain our observations, we postulated that ions pass through a confined pseudo-transition state as they cross the membrane−water interface that restricts the movement of both the cluster and any released water molecules to just 1 degree of translational freedom (forwards or backwards; Fig. 4D). After modifying the translational entropy terms in our DFT computed free energies and entropies to estimate the effects of confinement (see Methods), we found that dehydrating the ions to the required degree for permeation through AquaPIM results in a 0−30 kJ·mol^{-1} *decrease* in entropy (Fig. 4E, dashed lines), which is comparable to the range of activation entropies we obtained experimentally (–20 to −30 kJ·mol^{-1}; Fig. 2C). The corresponding free energy changes (~70 kJ·mol^{-1} for $\epsilon = 25$; Fig. 4D) have a similar magnitude to experimental activation free energies (~50 kJ·mol^{-1}; Fig. 2C); especially considering that the free energy is sensitive to the dielectric environment (see Fig. S22) and that $\epsilon = 25$ is an estimate. Strikingly, the entropy changes exhibit a greater variation among the ions than the corresponding free energy changes, which was also the case for our experimentally obtained activation free energies and suggests a degree of entropy-enthalpy compensation, as observed in other membrane systems.[25]

Our computational analysis of entropy changes thus indicates that dehydration of ions alone cannot account for the magnitudes or signs of the activation barriers obtained from experiment. Rather, confinement of ions plays a major role in dictating the magnitude of activation entropies and may account for differences in permeation behavior among similarly-charged ions. A recent study that also quantified single-ion energy barriers[36] reached a similar conclusion that dehydration alone cannot explain observed energy barriers for ion permeation. However, this study also suggested that dehydration effects still dominate partitioning barriers. By contrast, our findings indicate that confinement must be the cause.

Discussion

Identifying rate limitations in membrane transport

At first glance, our finding that crossing an interface has a higher free energy barrier than diffusion in both charged and uncharged membranes suggests that partitioning is "rate limiting," in contrast to assumptions embedded in the widely adopted solution–diffusion model.[1,22,23] However, rate limitations in membrane transport are more nuanced than those in chemical reactions (typically comprising no more than a few steps) due to the much larger number of discrete energy barriers in series (e.g., 100,000 barriers for a 50 µm thick membrane with λ=5 Å).[24,36]

The additive effects of many small barriers can add up to a substantially larger one when expressed on a macroscopic basis (i.e., $\Delta G_{ov,\delta}^{\ddagger,\mathrm{o}}$). For example, by Eq. 3, 100,000 barriers of 15 kJ·mol^{-1} in series have a combined $\Delta G_{ov,\delta}^{\ddagger,\mathrm{o}}$ of 43.5 kJ·mol^{-1}, while the microscsopic $\Delta G_{ov,\lambda}^{\ddagger,\mathrm{o}} = 15.07$ kJ·mol^{-1}. Hence, $\Delta G_{ov,\delta}^{\ddagger,\mathrm{o}}$ reflects the intuition that the energy barrier should increase with the length of the permeation pathway, while $\Delta G_{ov,\lambda}^{\ddagger,\mathrm{o}}$ does not. If one of the 15 kJ·mol^{-1} barriers is replaced with a larger barrier of 50 kJ·mol^{-1}, then $\Delta G_{ov,\delta}^{\ddagger,\mathrm{o}}$ increases to 50.2 kJ·mol^{-1} (Fig. 5A), again reflecting intuition that the overall energy barrier should be *at least* as large as the largest single free energy barrier. It is noteworthy that the combined effect of even 100,000 15 kJ·mol^{-1} barriers does not produce a $\Delta G_{ov,\delta}^{\ddagger,\mathrm{o}}$ as large as that of a single 50 kJ·mol^{-1} barrier. This counter-intuitive result is a result of the exponential relationship between rate and $\Delta G^{\ddagger}$. This example also illustrates that the microscopic barrier $\Delta G_{ov,\lambda}^{\ddagger,\mathrm{o}}$, with a value of only 21.6 kJ·mol^{-}

1, obfuscates the presence of the 50 kJ·mol^{-1} barrier. Previous studies that applied a kinetic approach to membrane transport[24,25,30,39] have relied exclusively on the *microscopic* free energy barrier to interpret results, potentially leading to incorrect conclusions about the relative importance of partitioning and diffusion. Nevertheless, it is unquestionably true that *diffusion plays a role* in determining the overall energy barrier. In this sense, our findings are not inconsistent with previous studies; [36] however, our work suggests that the role of partitioning compared to diffusion may be much greater than previously realized.

It has also been argued that diffusion must be rate limiting because the area-specific membrane resistance (ASR) and permeance are thickness-dependent [11], which we observed for both membranes we studied (Fig. S15-16). However, both the overall free energy barrier $\Delta G_{ov,\delta}^{\ddagger,o}$ and ASR predicted by Barrier Network Analysis increase with membrane thickness, *even though* $\Delta G_{sm}^{\ddagger,o} > \Delta G_m^{\ddagger,o}$ (Fig. S17; Eq. 2–3). The fact that ASR depends on thickness even when the partitioning barriers (~50 kJ·mol^{-1}; Fig. 3A) are much larger than the individual diffusion barriers (~18 kJ·mol^{-1}; Fig. 3A) is an illustration of the combined effects of many barriers in series described in the previous paragraph and Fig. 5A. Hence, thickness-dependence should not be misinterpreted as evidence that diffusion is rate-limiting.

In an attempt to generalize our findings, we quantified the relative contribution of partitioning to the overall rate of transport of a binary salt through hypothetical membranes with a range of $\Delta G_{ov,\delta}^{\ddagger,o}$ and thicknesses (Fig. 5B). We also overlay measured macroscopic energy barriers and thicknesses from this work and from various other membranes we converted from values reported in literature (see Supplemental Information). The partitioning contribution is defined as the ratio of overall to partitioning rate constants ($k_{ov,\delta}/k_{sm}$) and represents the degree (0–100%) to which partitioning controls the rate of transport. Since each rate constant is proportional to $\exp\frac{-\Delta G^{\ddagger}}{RT}$, the partitioning contribution is $\exp\frac{\Delta G_{sm}^{\ddagger,o}-\Delta G_{ov,\delta}^{\ddagger,o}}{RT}$ (see Eq. 2 and 3). Note that this formulation neglects the effects bulk diffusion, which was found to be unimportant relative to membrane diffusion. For reference, the example given in Fig 5A and discussed above has a partitioning contribution of 92%.

Fig. 5B shows that partitioning dominates the overall transport rate in most regions relevant to modern reverse osmosis, nanofiltration, and ion exchange membranes. Some of the thickest membranes (both ion exchange membranes, gray bars) straddle the region in which diffusion dominates the barrier (green), suggesting that there are important cases that are diffusion-limited. Note that Fig. 5B represents a total partition coefficient of 5, most appropriate for ion exchange membranes. Performing the same analysis for $K = 0.2$, which is more representative of microporous and RO/NF membranes (Fig. S18) shows that these membranes remain in the partitioning-dominated region.

Limitations and Generalizability

Although the analysis in Fig. 5B suggests that partitioning may constitute the rate limiting step in many more membranes beyond those tested here, we must acknowledge several important theoretical and practical limitations of our approach.

The equations of Barrier Network Analysis are valid for 1:1 salts of any charge and for transport driven by diffusion, applied electric fields, or applied pressure, and hence, could in principle be adapted to study rate limitations in many other membrane systems. However, development of these equations

involves several assumptions about microscopic phenomena inside the membrane, which are described in detail in the Supplemental Information. Briefly, these include 1) that all jumps have the same jump length λ, 2) that the applied driving forces (electric or pressure) across any individual barrier are small, 3) that all activation energy barriers are symmetric, 4) that the "no-recrossing" assumption of Transition State Theory applies, and 5) that the ratio between the activity coefficient of every ion and its transition state is similar throughout the system. Although we believe these assumptions to be well-justified and largely consistent with decades of prior work in the transition state theory literature, it is likely that many engineered membrane systems deviate from one or more of them. The degree to which such deviations quantitatively impact results is an important area for further study.

Integrating Barrier Network Analysis with experimental characterization to obtain single-ion energy barriers, as we have done in this work, requires additional assumptions that further restrict the practical systems to which this approach can be applied. First and foremost, we must neglect ion-ion interactions, allowing us to assume that energy barriers from single salt and mixed salt experiments are similar and that ions permeate independently of one another. The latter condition is clearly satisfied by electrically-driven transport, but would not be met in pressure-driven experiments where ions must permeate as "mobile salt" pairs. We also neglect ion pairing, which is reasonable for relatively low-concentration solutions of monovalent ions, but would not be justifiable in multivalent or highly concentrated solutions.

Lastly, although by construction we have neglected phenomena such as concentration polarization, ion pairing, or ion condensation, Barrier Network Analysis can in principle be extended to capture such effects. Equations 3 and 5 make it possible to create barrier networks of arbitrary complexity, much like constructing an equivalent circuit model to analyze impedance data. For example, phenomena such as ion pairing or counterion condensation could be included by adding a k_δ (and its constituent k_s, k_{sm}, k_m, and k_{ms} values) associated with a paired ion species or adding parallel rate process for condensed vs. uncondensed counter-ions inside the membrane, respectively.
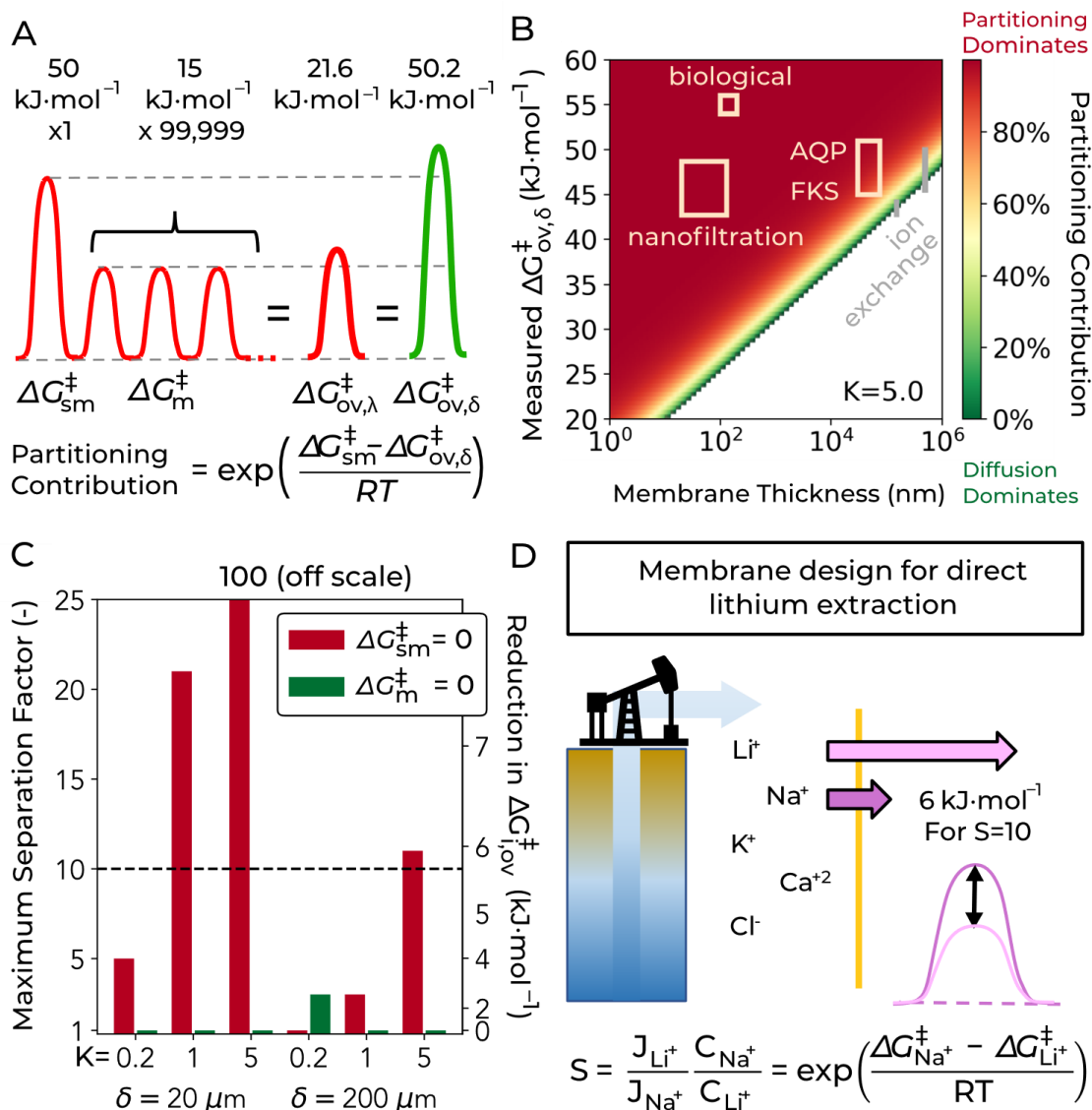
Figure 5: Application of Barrier Network Analysis to membrane design. (A) Combined effects of multiple activation free energy barriers in series, as represented by the microscopic or macroscopic overall free energy barriers, $\Delta G_{ov,\lambda}^{\ddagger,o}$ and $\Delta G_{ov,\delta}^{\ddagger,o}$. (B) Fraction of the overall permeation rate attributable to partitioning for various thicknesses and values of $\Delta G_{ov,\delta}^{\ddagger,o}$, where $\Delta G_m^{\ddagger,o} = 18$ kJ·mol^{-1}, $K = 5.0$, and the partitioning contribution is calculated as $k_{ov,\delta}/k_{sm}$ (see text). White regions indicate impossible combinations, i.e., areas in which the thickness of the membrane will result in a larger value of $\Delta G_{ov,\delta}^{\ddagger,o}$ than the one shown on the y axis. Boxed regions indicate reported ranges of thickness and energy barriers for salt transport in AquaPIM and FKS membranes (this work), nanofiltration membranes [46], ion exchange membranes [27,28,32], and for water transport in biological membranes [30]. (C) Maximum separation factor that can be achieved by modifying the hypothetical membrane of panel A to eliminate either the partitioning barrier ($\Delta G_{sm}^{\ddagger,o} = 0$) or diffusion barrier ($\Delta G_m^{\ddagger,o}=0$) for the target species. (D) Application of kinetic framework to direct lithium extraction from geothermal brine. To achieve a separation factor $S = 10$ for lithium, its $\Delta G_{i,\delta}^{\ddagger,o}$ must be approximately 6 kJ·mol^{-1} lower than that of competing species such as sodium.

Implications for membrane design

The fact that partitioning may often have a higher energy barrier than diffusion has significant implications for membrane design. To achieve single-ion separation for applications such as direct lithium extraction, it is necessary to lower $\Delta G_{i,\delta}^{\ddagger,o}$ for a specific target species (e.g., Li$^+$) relative to others. Eq. 1 provides a direct quantitative connection between the difference in free energy barriers and the corresponding separation factor S that would be achieved in membrane transport (Fig. 5D). For example, according to Eq. 1, lowering the barrier for a target species by 5.7 kJ·mol^{-1} relative to others would result in a separation factor of approximately 10. This value is comparable to the differences in binding Na$^+$ and K$^+$ binding energies to 18-crown-6 in methanol,[47] suggesting that host-guest chemistries may offer a feasible path to ion-specific selectivity. However, the extent to which such chemistries could be used to affect the interfacial activation free energy $\Delta G_{sm}^{\ddagger,o}$ remains unclear.

To connect separation factor to microscopic membrane design strategies, we turn to Eq. 2 and calculate the maximum separation factor that could be achieved by modifying a membrane similar to those studied here to eliminate (set to zero) either the (de)partitioning barrier or the diffusion barrier (Fig. 5C). Eliminating the partitioning barrier results in high separation factors when 1) the membrane is relatively thin and/or 2) the partition coefficients are relatively large (K = 1 to 5). By contrast, eliminating the diffusion barrier results in little to no improvement in the separation factor. Therefore, focusing research efforts on chemical or physical strategies that lower the partitioning energy barrier of a target ion by 5 to 10 kJ·mol^{-1} relative to competing ions may have a greater impact on membrane performance than engineering the bulk of the membrane.

Conclusion and Outlook

In summary, we have developed a flexible and general kinetic framework to analyze ion transport and used it to determine that partitioning, not diffusion, has the largest activation energy barrier for alkali chloride transport in microporous AquaPIM and highly-charged FKS, which represent two classes of engineered membranes relevant to modern ion separations. Our finding challenges historical assumptions embedded in the solution-diffusion model and suggests that efforts to engineer membranes for improved single-ion selectivity should give greater attention to ion-specific surface interactions. Although Barrier Network Analysis can only be fully applied to selected systems subject to limiting assumptions, it nevertheless provides a powerful, quantitative framework for rationalizing ion-specific selectivity trends and for testing hypotheses about selective membrane design.

Experimental Procedures

Resource Availability

Lead Contact
Questions or requests for further information about this work should be directed to the lead contact, Prof. Ryan Kingsbury (kingsbury@princeton.edu).

Materials availability
This study did not generate new materials. Further details about the synthesis of AquaPIM membranes can be found in Baran et al.[19]

Data and Code availability
Original data not already included in the Supplemental Information is available upon reasonable request.

Membranes

AquaPIM polymer solution (M_n = 124 kg·mol^{-1}, M_w = 137 kg·mol^{-1}) was synthesized as previously described [19]. To cast AquaPIM membranes, a 12.5 mg·mL^{-1} polymer ink was first prepared by stirring AquaPIM in dimethyl sulfoxide at room temperature for 16 h, at which point it was fully dissolved. Next, 2 mL of polymer ink was pipetted into a Teflon well with a diameter of 3.5 cm and depth of 1 cm. The solvent evaporated for 48 h in a 120 °C oven, producing a flexible and transparent membrane. Prior to testing, fresh cast AquaPIM membranes were conditioned by soaking in 1 M KOH base solution for 24 h to improve wettability. After soaking in base, the membranes were placed in deionized water for a minimum of 1 h, then in the respective electrolyte solutions for a minimum of 48 h, during which the solutions were exchanged at least twice to remove any residual base.

Commercial FKS-50 cation exchange membranes (FumaTech GmbH) were purchased and conditioned according to the manufacturer's instructions. The as-received dry film was first placed in DI water at 60 C for 5 h, after which circular membrane coupons were punched from the film and placed in 0.3 M hydrochloric acid for 30 min. Acid-conditioned membrane coupons were next soaked in DI water for 30 min prior to being placed in electrolyte solutions, exchanging the water one time. Commercial membrane coupons were soaked in the respective electrolyte solutions for a minimum of 48hr prior to any testing, during which the solutions were exchanged at least twice.

Electrolyte Solutions

Electrolyte solutions comprising 0.1 M LiCl, NaCl, or KCl were prepared from ACS-grade reagents and DI water. A mixed solution with same total ion concentration, containing 0.033 M each of LiCl, NaCl, and KCl was prepared in analogous fashion. All electrolytes were adjusted to pH 5 using dilute HCl and HEPES buffer. This pH was chosen to maximize metal cation solubility while ensuring that the amidoxime groups on the AquaPIM remained uncharged (amidoxime pKa $\approx$ 4 [19,48]) and because AquaPIM membranes were previously observed to become brittle at pH below 4 [19].

Ionic conductivity

Ionic conductivity was measured using the through-plane, direct contact technique described by Diaz et al [49]. Membranes were removed from electrolyte solution and installed in a Controlled Environment

---

Sample Holder (CESH; Bio-Logic, Inc.) between two 2-cm diameter gold electrodes, such that the membrane covered the entirety of the electrode surface. A digital micrometer (Mahr 1086R) installed on the sample holder allowed measurement of the membrane thickness as the apparatus was being tightened; the thumbscrew controlling the spacing between the electrodes was tightened until the membrane thickness stabilized. The sample holder was connected to a potentiostat (Bio-Logic VMP3) which applied an oscillating potential of 10 mV over a frequency range of 3 MHz to 100 Hz. Short-circuit impedance was obtained from a measurement using the same settings in which the electrodes were clamped together with no membrane present; this measurement was used to correct all obtained spectra for inductive effects arising from the test apparatus. Open circuit compensation was also evaluated but found to be unnecessary. The conductivity was obtained as the real intercept of the background-corrected Nyquist plots.

Free Energy of Activation

The free energy of activation for ion permeation, $\Delta G_{ov}^{\ddagger,o}$, was obtained by performing impedance spectroscopy measurements at different temperatures. The CESH apparatus described in the previous section was placed in an environmental chamber and conductivity measurements were taken at 25, 35, 45, and 55 °C. The temperature was held at the specified value until the conductivity reading stabilized, indicating that the membrane sample had warmed to the target temperature. $\Delta G_{ov}^{\ddagger,o}$ was obtained from plots of conductivity vs. temperature, as described in detail in the Supplemental Information.

Partition coefficients and water uptake

Partition coefficients and water uptake were obtained via methods reported previously [50]. Following conductivity measurements, the same membrane coupons were removed from their respective electrolyte solutions, blotted dry to remove surface moisture, weighed, and placed into 10 mL DI water at 25 C, causing sorbed cations and anions ("mobile salt") to desorb from the membrane. Partition coefficients at other temperatures were obtained by placing the membrane coupon back into electrolyte solution for at least 24 h and desorbing in DI water for at least 48 h, with both steps carried out at temperatures of 35, 45, and 55 °C. Note that the ions desorbed in this manner represent co-ions or "mobile salt" that are not associated with fixed charge sites on the membrane. The AquaPIM membranes in this work were uncharged at pH 5 [19,48], and hence were not expected to contain any significant population of counter-ions associated to charged sites. On the other hand the FKS membrane contains a high concentration of negatively-charged sites. To measure the population of ions associated with fixed charge sites, after completing the desorption tests in water described above, we placed the membrane coupon in a solution of 2% nitric acid to cause any remaining ions to desorb into the acid by ion exchange.

The concentration of cations in the desorption solution was subsequently analyzed using inductively coupled plasma–optical emission spectrometry (ICP–OES). Meanwhile, the membrane coupons were removed from the acid, placed back into DI water for 48 h, dried in a convection oven at 60 C for 24 h, and weighed. The wet and dry weights of the membranes were used to determine their water uptake according to

$$w.u. = \frac{m_{wet} - m_{dry}}{m_{dry}} \tag{8}$$

---

where m_{wet} and m_{dry} are the wet and dry masses, respectively. Using the water uptake and the measured cation concentrations in the desorption solution, the membrane-phase concentration of cations $\overline{C_i}$ (mol·L^{-1} of water absorbed by the membrane) was determined as

$$\overline{C_i} = \frac{C_i V_w \rho_w}{m_{wet} - m_{dry}} \qquad (9)$$

where C_i (mol·L^{-1}) is the ion concentration in the desorption solution, V_w (10 mL) is the volume of desorption solution, and ρ_w (0.998 g·mL^{-1}) is the density of water.

Finally, we calculated the partition coefficient of ion i as

$$K_i = \frac{\overline{C_i}}{C_i} \left(\frac{w.u.}{w.u. + \frac{\rho_w}{\rho_p}} \right) \qquad (10)$$

where the factor $\left(\frac{w.u.}{w.u. + \frac{\rho_w}{\rho_p}} \right)$ is the volume fraction of water in the membrane, which converts the concentration $\overline{C_i}$ from units of mol·L^{-1} of water absorbed by the membrane to mol·L^{-1} swollen membrane, which is the appropriate unit of measure when calculating partition coefficients [50,51]. To perform this conversion, we assumed density of dry polymer, $\rho_p = 1.15$ g·mL^{-1} [50].

Because both AQP and FKS membranes were either neutral or negatively charged, the total concentration of chloride anions sorbed by the membranes must be equal to the mobile cation concentration by electroneutrality. Hence, Cl$^-$ partition coefficients were calculated from the sum of the membrane-phase mobile cation concentrations.

Electrodialysis

Electrodialysis was conducted in a two-compartment glass H-cell obtained from Adams and Chittenden (Berkeley, CA). The general experimental setup is shown in Fig. S13. Preconditioned membranes were held in place with a Teflon and rubber gasket with an inside diameter of 15 mm, resulting in an exposed (active) membrane area of 1.76 cm^2. The feed solution was an aqueous buffered electrolyte comprised of 0.033 M LiCl, 0.033 M NaCl, and 0.033 M KCl, of which 15 mL was added to the anodic half-cell. The receiving solution was aqueous 0.1 M tetrabutylammonium chloride, of which 15 mL was added to the cathodic half-cell. Both half cells were equipped with carbon paper electrodes with an area of 4 cm^2. A Teflon coated stir bar was placed in both feed and permeate compartments to provide mixing. A 20 mA direct current was passed between the electrodes, causing cations to migrate into the receiving chamber and anions to permeate in the opposite direction. 200 μL aliquots of the receiving solution were taken at time points of 0, 10, 20, and 30 min and diluted to 4 mL total volume. Cation concentrations in the diluted aliquots were determined by inductively coupled plasma - optical emission spectrometry (ICP-OES).

Significant gas evolution occurred at both electrodes, resulting in pH changes in both solutions during the experiment. As a result, plots of total ion transport vs. total current passed (Fig. S14) were nonlinear due to an increasing fraction of current being carried by protons. To minimize the effect of proton

transport on our analysis, we determined the ion transport numbers from the initial slope, obtained from the data at t=0 and t=10 min.

Computational Procedures

Density Functional Theory (DFT) Simulations

Initial structures for hydrated ions were generated using the Quantum Cluster Growth[52] algorithm in the CREST software[53] to place between 1 and 20 explicit H_2O molecules around the central ion. Briefly, this algorithm builds solvated clusters using a semi-empirical electronic structure method, an implicit solvent model, and a restraining potential. All clusters were grown using implicit water as the surrounding solvent, and the obtained geometries were taken as the input for subsequent density functional theory (DFT) simulations.

DFT simulations comprised an initial structure optimization using the ωB97X-D[54] functional with def2-SVPD[55] basis and a polarizable continuum model (PCM) implicit dielectric of either 5, 25, or 78.4. Dielectric constants of 5 and 25 were chosen to bracket the range of measured dielectric permittivity of water inside several ion-conducting polymers at similar water contents to the membranes used here.[44]

After initial optimization, we utilized the frequency flattening optimization workflow implemented in atomate[56] to obtain vibrational frequencies at the same level of theory (ωB97X-D/def2-SVPD/PCM). This workflow first performs a frequency calculation, then checks whether there are any imaginary frequency modes present. If imaginary modes are found, the geometry is perturbed slightly and re-optimized. The process is repeated until there are no imaginary frequencies remaining, indicating that a true minimum on the potential energy surface has been found. This procedure was successful for the great majority of partially dehydrated ions (i.e., all imaginary modes were eliminated); however, in the case of clusters involving Cl^-, numerous imaginary modes remained, likely because of the lower charge density and relatively weaker binding of water molecules to anions compared to the alkali cations. Following the frequency flattening procedure, we then performed a single-point energy calculation on the final geometry using the ωB97X-V[57] functional with def2-TZVPD[58] basis set. All calculations were performed in Q-Chem[59] version 5.4. The free energy of each cluster at 298 K, G^{298}, was calculated according to
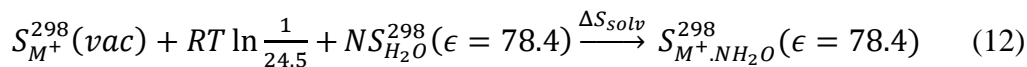
$$G^{298} = E + H^{0\rightarrow298} - TS^{298} \tag{11}$$

where E is the electronic energy from the single point calculation, $H^{0\rightarrow298}$ is the change in enthalpy from 0 to 298 K, and S^{298} is the (absolute) entropy at 298 K, comprising translational, rotational, vibrational, and electronic contributions. $H^{0\rightarrow298}$ and S^{298} were calculated from the vibrational frequencies via the quasi-rigid-rotor-harmonic oscillator (QRRHO) approach.[60]

The free energy of water, G_{H2O}, was obtained via the same calculation procedure using clusters of 1 to 20 water molecules. To account for the different concentrations of water clusters relative to the standard state (1 M), we added a concentration correction of $RT \ln \frac{55.5}{n}$ to G^{298}, where n is the number of water molecules in the cluster.[61] We analyzed a total of 23 water clusters, obtained from either classical molecular dynamics or the QCG procedure used to generate the solvated ions. G_{H_2O} converged to a constant value as the cluster size increased (Fig. S19). The final value of G_{H_2O} was taken from the largest

---

cluster that had no remaining imaginary frequencies, which corresponded to $n = 12$. The DFT-computed S_{H_2O} was 18.30 kJ·mol^{-1}, in reasonable agreement with the experimental value of 20.86 kJ·mol^{-1}.[62]

Next, we determined the number of explicit water molecules corresponding to full hydration of each ion, N, as the value that reproduced the experimental solvation entropies as accurately as possible, according to the reaction:

$$S_{M^+}^{298}(vac) + RT \ln \frac{1}{24.5} + NS_{H_2O}^{298}(\epsilon = 78.4) \xrightarrow{\Delta S_{solv}} S_{M^+.NH_2O}^{298}(\epsilon = 78.4) \quad (12)$$

where (vac) and $(\epsilon = 78.4)$ denote quantities calculated in vacuum and in implicit solvent, respectively. The quantity $RT \ln \frac{1}{24.5}$ corrects the gas-phase entropy from a standard state of 1 atm to 1 mol·L^{-1}, for consistency with the aqueous energies. The calibrated values of N were 16, 15, 14, and 10 H_2O for Li$^+$, Na$^+$, K$^+$, and Cl$^-$ ions, respectively.

Using these values, the DFT-computed solvation entropies and free energies for cations reproduced experimental values to within 6% and 8.6%, respectively (Fig. S20 and S21). For Cl$^-$, the computed solvation entropy deviated from experiment by 26%, but the solvation free energy was accurate to within 2%. The large deviation in entropy from experiment was likely related to the presence of imaginary frequency modes in the Cl$^-$ clusters, as discussed above.

Partial Dehydration Energies

We used the computed energies and entropies of hydrated ions and water to estimate the changes in free energy and entropy associated with the transfer and partial dehydration of ions from the fully hydrated, bulk state into a lower dielectric medium representative of a polymer membrane. This process is represented by the reaction:

$$M^+.N\ H_2O(\epsilon = 78.4) \xrightarrow{\Delta G,\ \Delta S} M^+.nH_2O(\epsilon = 5, 25) + (N - n)H_2O(\epsilon = 78.4) \quad (13)$$
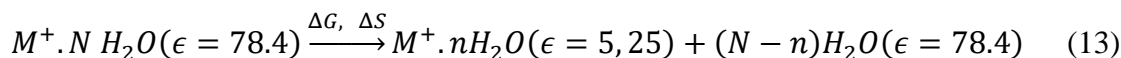
where M^+ denotes the cation, N and n represent the number of water molecules associated with a fully hydrated ion in water and with the partially dehydrated ion, respectively, and the ϵ in parentheses indicates the dielectric environment of the species. Note that by construction, our estimated partial dehydration energies assume that water molecules are released into the bulk solution.

Confinement

The effects of confinement on the ΔG and ΔS of partial dehydration (see previous section) were estimated by reducing the translational entropy of the partially dehydrated clusters (species $M^+.nH_2O$ in Eq. 13). The translational entropy component of S^{298} is given by the Sackur–Tetrode equation[63]

$$S^{trans} = R \left[\ln \left(L \sqrt{\frac{2k_bT\pi m}{N_A h^2}} \right)^{DOF} + 1 + \frac{DOF}{2} \right] \quad (14)$$

where L is the length that is available for the cluster to translate along each degree of freedom, m is the mass of the cluster, h (6.626x10^{-34} J·Hz^{-1}) is the Planck constant, k_b is the Boltzmann constant, and DOF is an integer 1, 2, or 3 describing the degrees of translational freedom.

By default, all DFT computed entropies set $DOF = 3$ and reflect an L corresponding to the distance between particles in an ideal gas (34 Å). To estimate confinement, we re-computed S^{trans} with $DOF = 2$ and $DOF = 1$, and with smaller distances L of 8.6 Å or 5.6 Å, corresponding to the pore sizes inside AquaPIM. We then subtracted the original S^{trans} from the DFT computed S^{298} and added the adjusted value of S^{trans} to obtain new estimates of the free energy and entropy changes.

Ion Cluster Size

The effective sizes of fully and partially hydrated ions were estimated based on the diameter of the minimal enclosing cylinder bounding a region defined by the Van der Waals radii of hydrogen and oxygen and the ionic radius of the respective ions, which are listed in Table S1.

References

1. Geise, G.M., Paul, D.R., and Freeman, B.D. (2014). Fundamental water and salt transport properties of polymeric materials. Progress in Polymer Science *39*, 1–42. 10.1016/j.progpolymsci.2013.07.001.

2. Patel, S.K., Biesheuvel, P.M., and Elimelech, M. (2021). Energy Consumption of Brackish Water Desalination: Identifying the Sweet Spots for Electrodialysis and Reverse Osmosis. ACS ES&T Engineering. 10.1021/acsestengg.0c00192.

3. Biesheuvel, P.M., Porada, S., Elimelech, M., and Dykstra, J.E. (2022). Tutorial review of reverse osmosis and electrodialysis. Journal of Membrane Science *647*, 120221. 10.1016/j.memsci.2021.120221.

4. Kingsbury, R.S., Wang, J., and Coronell, O. (2020). Comparison of water and salt transport properties of ion exchange, reverse osmosis, and nanofiltration membranes for desalination and energy applications. Journal of Membrane Science *604*. 10.1016/j.memsci.2020.117998.

5. Luo, T., Abdu, S., and Wessling, M. (2018). Selectivity of ion exchange membranes: A review. Journal of Membrane Science *555*, 429–454. 10.1016/j.memsci.2018.03.051.

6. Foo, Z.H., Rehman, D., Bouma, A.T., Monsalvo, S., and Lienhard, J.H. (2023). Lithium Concentration from Salt-Lake Brine by Donnan-Enhanced Nanofiltration. Environ. Sci. Technol. *57*, 6320–6330. 10.1021/acs.est.2c08584.

7. Lounder, S.J., and Asatekin, A. (2021). Zwitterionic Ion-Selective Membranes with Tunable Subnanometer Pores and Excellent Fouling Resistance. Chem. Mater. *33*, 4408–4416. 10.1021/acs.chemmater.1c00374.

8. Fan, H., Huang, Y., and Yip, N.Y. (2023). Advancing ion-exchange membranes to ion-selective membranes: principles, status, and opportunities. Front. Environ. Sci. Eng. *17*, 25. 10.1007/s11783-023-1625-0.

9. Sujanani, R., Landsman, M.R., Jiao, S., Moon, J.D., Shell, M.S., Lawler, D.F., Katz, L.E., and Freeman, B.D. (2020). Designing Solute-Tailored Selectivity in Membranes: Perspectives for Water Reuse and Resource Recovery. ACS Macro Letters, 1709–1717. 10.1021/acsmacrolett.0c00710.

10. DuChanois, R.M., Cooper, N.J., Lee, B., Patel, S.K., Mazurowski, L., Graedel, T.E., and Elimelech, M. (2023). Prospects of metal recovery from wastewater and brine. Nat Water *1*, 37–46. 10.1038/s44221-022-00006-z.

11. DuChanois, R.M., Heiranian, M., Yang, J., Porter, C.J., Li, Q., Zhang, X., Verduzco, R., and Elimelech, M. (2022). Designing polymeric membranes with coordination chemistry for high-precision ion separations. Sci. Adv. *8*, eabm9436. 10.1126/sciadv.abm9436.

12. Dong, Y., Liu, Y., Li, H., Zhu, Q., Luo, M., Zhang, H., Ye, B., Yang, Z., and Xu, T. (2023). Crown ether-based Tröger's base membranes for efficient Li+/Mg2+ separation. Journal of Membrane Science *665*, 121113. 10.1016/j.memsci.2022.121113.

---

13. Yang, Z., Guo, R., Malpass-Evans, R., Carta, M., McKeown, N.B., Guiver, M.D., Wu, L., and Xu, T. (2016). Highly Conductive Anion-Exchange Membranes from Microporous Tröger's Base Polymers. Angew. Chem. Int. Ed. *55*, 11499–11502. 10.1002/anie.201605916.

14. Warnock, S.J., Sujanani, R., Zofchak, E.S., Zhao, S., Dilenschneider, T.J., Hanson, K.G., Mukherjee, S., Ganesan, V., Freeman, B.D., Abu-Omar, M.M., et al. (2021). Engineering Li/Na selectivity in 12-Crown-4–functionalized polymer membranes. Proc Natl Acad Sci USA *118*, e2022197118. 10.1073/pnas.2022197118.

15. Uliana, A.A., Bui, N.T., Kamcev, J., Taylor, M.K., Urban, J.J., and Long, J.R. (2021). Ion-capture electrodialysis using multifunctional adsorptive membranes. Science *372*, 296–299.

16. Carey, C., Díaz, J.C., Kitto, D., Espinoza, C., Ahn, E., and Kamcev, J. (2023). Interfacial interactions between polymers and selective adsorbents influence ion transport properties of boron scavenging ion-exchange membranes. Journal of Membrane Science *669*, 121301. 10.1016/j.memsci.2022.121301.

17. Tan, R., Wang, A., Malpass-Evans, R., Williams, R., Zhao, E.W., Liu, T., Ye, C., Zhou, X., Darwich, B.P., Fan, Z., et al. (2020). Hydrophilic microporous membranes for selective ion separation and flow-battery energy storage. Nat. Mater. *19*, 195–202. 10.1038/s41563-019-0536-8.

18. Zuo, P., Li, Y., Wang, A., Tan, R., Liu, Y., Liang, X., Sheng, F., Tang, G., Ge, L., Wu, L., et al. (2020). Sulfonated Microporous Polymer Membranes with Fast and Selective Ion Transport for Electrochemical Energy Conversion and Storage. Angew. Chem. Int. Ed. *59*, 9564–9573. 10.1002/anie.202000012.

19. Baran, M.J., Braten, M.N., Sahu, S., Baskin, A., Meckler, S.M., Li, L., Maserati, L., Carrington, M.E., Chiang, Y.M., Prendergast, D., et al. (2019). Design Rules for Membranes from Polymers of Intrinsic Microporosity for Crossover-free Aqueous Electrochemical Devices. Joule *3*, 2968–2985. 10.1016/j.joule.2019.08.025.

20. Zuo, P., Ye, C., Jiao, Z., Luo, J., Fang, J., Schubert, U.S., McKeown, N.B., Liu, T.L., Yang, Z., and Xu, T. (2023). Near-frictionless ion transport within triazine framework membranes. Nature. 10.1038/s41586-023-05888-x.

21. Lounder, S.J., and Asatekin, A. (2021). Interaction-based ion selectivity exhibited by self-assembled, cross-linked zwitterionic copolymer membranes. Proc. Natl. Acad. Sci. U.S.A. *118*, e2022198118. 10.1073/pnas.2022198118.

22. Wijmans, J.G., and Baker, R.W. (1995). The solution-diffusion model: a review. Journal of Membrane Science *107*, 1–21. 10.1016/0376-7388(95)00102-I.

23. Paul, D.R. (2004). Reformulation of the solution-diffusion theory of reverse osmosis. Journal of Membrane Science *241*, 371–386. 10.1016/j.memsci.2004.05.026.

24. Shefer, I., Lopez, K., Straub, A.P., and Epsztein, R. (2022). Applying Transition-State Theory to Explore Transport and Selectivity in Salt-Rejecting Membranes: A Critical Review. Environ. Sci. Technol. *56*, 7467–7483. 10.1021/acs.est.2c00912.

---

25. Shefer, I., Peer-Haim, O., and Epsztein, R. (2022). Limited ion-ion selectivity of salt-rejecting membranes due to enthalpy-entropy compensation. Desalination *541*, 116041. 10.1016/j.desal.2022.116041.

26. Samanta, T. (2003). Physico-chemical aspects of some biological membranes. II. Colloids and Surfaces B: Biointerfaces *27*, 95–101. 10.1016/S0927-7765(02)00046-2.

27. Samanta, T., and Basu, A.S. (1987). Conductance behaviour of a microporous membrane and the application of absolute reaction rate theory. Journal of Membrane Science *31*, 89–102. 10.1016/S0376-7388(00)81342-3.

28. Samanta, T., and Basu, A.S. (1989). Studies of the conductances of potassium halides, halates, and nitrate in aqueous solutions in a microporous membrane and the application of absolute reaction rate theory. Journal of Membrane Science *45*, 247–260. 10.1016/S0376-7388(00)80517-7.

29. Beg, M.N., Ahmad, K., Altaf, I., and Arshad, M. (1981). Ionic transport of alkali chlorides in parchment supported cupric orthophosphate membrane and application of absolute reaction rate theory. Journal of Membrane Science *9*, 303–311. 10.1016/S0376-7388(00)80271-9.

30. Zwolinski, B.J., Eyring, H., and Reese, C.E. (1949). Diffusion and Membrane Permeability. I. J. Phys. Chem. *53*, 1426–1453. 10.1021/j150474a012.

31. Parsegian, A. (1969). Energy of an ion crossing a low dielectric membrane: Solutions to four relevant electrostatic problems. Nature *224*, 844–846. 10.1038/224488a0.

32. Epsztein, R., Shaulsky, E., Qin, M., and Elimelech, M. (2019). Activation behavior for ion permeation in ion-exchange membranes: Role of ion dehydration in selective transport. Journal of Membrane Science *580*, 316–326. 10.1016/j.memsci.2019.02.009.

33. Rickman, M., Davis, R.H., and Pellegrino, J. (2014). Temperature-variation study of neutral solute and electrolyte fractionation through cellulose acetate and polyamide membranes. Journal of Membrane Science *461*, 114–122. 10.1016/j.memsci.2014.03.023.

34. Sharma, R.R., and Chellam, S. (2006). Temperature and concentration effects on electrolyte transport across porous thin-film composite nanofiltration membranes: Pore transport mechanisms and energetics of permeation. Journal of Colloid and Interface Science *298*, 327–340. 10.1016/j.jcis.2005.12.033.

35. Kamcev, J., Galizia, M., Benedetti, F.M., Jang, E.-S., Paul, D.R., Freeman, B., and Manning, G.S. (2016). Partitioning of Mobile Ions Between Ion Exchange Polymers and Aqueous Salt Solutions: Importance of Counter-ion Condensation. Phys. Chem. Chem. Phys., 6021–6031. 10.1039/C5CP06747B.

36. Zhou, X., Wang, Z., Epsztein, R., Zhan, C., Li, W., Fortner, J.D., Pham, T.A., Kim, J.H., and Elimelech, M. (2020). Intrapore energy barriers govern ion transport and selectivity of desalination membranes. Science Advances *6*. 10.1126/sciadv.abd9045.

37. Fennell, C.J., Bizjak, A., Vlachy, V., and Dill, K.A. (2009). Ion Pairing in Molecular Simulations of Aqueous Alkali Halide Solutions. J. Phys. Chem. B *113*, 6782–6791. 10.1021/jp809782z.

38. Chen, A.A., and Pappu, R.V. (2007). Quantitative Characterization of Ion Pairing and Cluster Formation in Strong 1:1 Electrolytes. J. Phys. Chem. B *111*, 6469–6478. 10.1021/jp0708547.

39. Gray-Weale, A.A., Henchman, R.H., Gilbert, R.G., Greenfield, M.L., and Theodorou, D.N. (1997). Transition-State Theory Model for the Diffusion Coefficients of Small Penetrants in Glassy Polymers. Macromolecules *30*, 7296–7306. 10.1021/ma970349f.

40. Oelkers, E.H., and Helgeson, H.C. (1988). Calculation of the thermodynamic and transport properties of aqueous species at high pressures and temperatures: Aqueous tracer diffusion coefficients of ions to 1000°C and 5 kb. Geochimica et Cosmochimica Acta *52*, 63–85. 10.1016/0016-7037(88)90057-9.

41. Mackie, J.S., and Meares, P. (1955). The Diffusion of Electrolytes in a Cation-Exchange Resin Membrane. I. Theoretical. Proceedings of the Royal Society of London A *232*, 498–509.

42. Mackie, J.S., and Meares, P. (1955). The Diffusion of Electrolytes in a Cation-Exchange Resin Membrane . II . Experimental. Proceedings of the Royal Society of London A *232*, 510–518.

43. Baran, M.J., Carrington, M.E., Sahu, S., Baskin, A., Song, J., Baird, M.A., Han, K.S., Mueller, K.T., Teat, S.J., Meckler, S.M., et al. (2021). Diversity-oriented synthesis of polymer membranes with ion solvation cages. Nature *592*, 225–231. 10.1038/s41586-021-03377-7.

44. Chang, K., and Geise, G.M. (2019). Dielectric Permittivity Properties of Hydrated Polymers: Measurement and Connection to Ion Transport Properties. Industrial and Engineering Chemistry Research. 10.1021/acs.iecr.9b03950.

45. Glasstone, S., Laidler, Keith J., and Eyring, H. (1941). The theory of rate processes: the kinetics of chemical reactions, viscosity, diffusion and electrochemical phenomena 1st ed. (McGraw-Hill Book Company, Inc.).

46. Shefer, I., Peer-Haim, O., Leifman, O., and Epsztein, R. (2021). Enthalpic and Entropic Selectivity of Water and Small Ions in Polyamide Membranes. Environ. Sci. Technol. *55*, 14863–14875. 10.1021/acs.est.1c04956.

47. Inoue, Y., Liu, Y., Tong, L.-H., Ouchi, M., and Hakushi, T. (1993). Complexation thermodynamics of crown ethers. Part 3. 12-Crown-4 to 36-crown-12: from rigid to flexible ligand. J. Chem. Soc., Perkin Trans. 2, 1947. 10.1039/p29930001947.

48. Mehio, N., Lashely, M.A., Nugent, J.W., Tucker, L., Correia, B., Do-Thanh, C.-L., Dai, S., Hancock, R.D., and Bryantsev, V.S. (2015). Acidity of the Amidoxime Functional Group in Aqueous Solution: A Combined Experimental and Computational Study. J. Phys. Chem. B *119*, 3567–3576. 10.1021/jp512778x.

49. Díaz, J.C., and Kamcev, J. (2021). Ionic conductivity of ion-exchange membranes: Measurement techniques and salt concentration dependence. Journal of Membrane Science *618*. 10.1016/j.memsci.2020.118718.

50. Kingsbury, R.S., Zhu, S., Flotron, S., and Coronell, O. (2018). Microstructure determines water and salt permeation in commercial ion exchange membranes. ACS Applied Materials & Interfaces *10*, 39745–39756. 10.1021/acsami.8b14494.

51. Kamcev, J., Paul, D.R., Manning, G.S., and Freeman, B.D. (2017). Predicting Salt Permeability Coefficients in Highly Swollen, Highly Charged Ion Exchange Membranes. ACS Applied Materials & Interfaces *9*, 4044–4056. 10.1021/acsami.6b14902.

52. Spicher, S., Plett, C., Pracht, P., Hansen, A., and Grimme, S. (2022). Automated Molecular Cluster Growing for Explicit Solvation by Efficient Force Field and Tight Binding Methods. J. Chem. Theory Comput. *18*, 3174–3189. 10.1021/acs.jctc.2c00239.

53. Grimme, S. (2019). Exploration of Chemical Compound, Conformer, and Reaction Space with Meta-Dynamics Simulations Based on Tight-Binding Quantum Chemical Calculations. Journal of Chemical Theory and Computation *15*, 2847–2862. 10.1021/acs.jctc.9b00143.

54. Chai, J.-D., and Head-Gordon, M. (2008). Long-range corrected hybrid density functionals with damped atom–atom dispersion corrections. Phys. Chem. Chem. Phys. *10*, 6615. 10.1039/b810189b.

55. Rappoport, D., and Furche, F. (2010). Property-optimized Gaussian basis sets for molecular response calculations. The Journal of Chemical Physics *133*, 134105. 10.1063/1.3484283.

56. Mathew, K., Montoya, J.H., Faghaninia, A., Dwarakanath, S., Aykol, M., Tang, H., Chu, I., Smidt, T., Bocklund, B., Horton, M., et al. (2017). Atomate: A high-level interface to generate, execute, and analyze computational materials science workflows. Computational Materials Science *139*, 140–152. https://doi.org/10.1016/j.commatsci.2017.07.030.

57. Mardirossian, N., and Head-Gordon, M. (2014). ωB97X-V: A 10-parameter, range-separated hybrid, generalized gradient approximation density functional with nonlocal correlation, designed by a survival-of-the-fittest strategy. Phys. Chem. Chem. Phys. *16*, 9904. 10.1039/c3cp54374a.

58. Weigend, F., and Ahlrichs, R. (2005). Balanced basis sets of split valence, triple zeta valence and quadruple zeta valence quality for H to Rn: Design and assessment of accuracy. Phys. Chem. Chem. Phys. *7*, 3297. 10.1039/b508541a.

59. Shao, Y., Gan, Z., Epifanovsky, E., Gilbert, A.T.B., Wormit, M., Kussmann, J., Lange, A.W., Behn, A., Deng, J., Feng, X., et al. (2015). Advances in molecular quantum chemistry contained in the Q-Chem 4 program package. Molecular Physics *113*, 184–215. 10.1080/00268976.2014.952696.

60. Grimme, S. (2012). Supramolecular Binding Thermodynamics by Dispersion-Corrected Density Functional Theory. Chem. Eur. J. *18*, 9955–9964. 10.1002/chem.201200497.

61. Itkis, D., Cavallo, L., Yashina, L.V., and Minenkov, Y. (2021). Ambiguities in solvation free energies from cluster-continuum quasichemical theory: lithium cation in protic and aprotic solvents. Phys. Chem. Chem. Phys. *23*, 16077–16088. 10.1039/D1CP01454D.

62. Cox, J.D., Wagman, D.D., and Medvedev, V.A. (1989). CODATA KEY VALUES FOR THERMODYNAMICS (Hemisphere Publishing Corp).

63. Garza, A.J. (2019). Solvation Entropy Made Simple. J. Chem. Theory Comput. *15*, 3204–3214. 10.1021/acs.jctc.9b00214.

Writing – original draft: RSK

Writing – review & editing: RSK, MAB, BAH, EH

Competing interests: R.S.K. has a financial interest in Membrion, Inc. B.A.H. has a financial interest in Sepion Technologies and Cyklos Materials. The other authors declare that they have no competing interests.

Data and materials availability: All data are available in the main text or the Supplemental Information.

Supplemental Information

Supplemental Text
Figs. S1 to S32
Tables S1 to S9